Accepted to Phys. Fluids 10.1063/5.0170251

On Computational Simulations of Dynamic Stall and Its Three-Dimensional Nature

Nabil M. Khalifa,[1] Amirsaman Rezaei,[1] and Haithem E. Taha[1]
Mechanical and Aerospace Engineering, University of California, Irvine, CA 92697, USA.

(*Electronic mail: nkhalifa@uci.edu)

(Dated: 16 September 2023)

In this paper, we investigate the three-dimensional nature of dynamic stall. Conducting the investigation, the flow around a harmonically pitching National Advisory Committee for Aeronautics (NACA) 0012 airfoil is numerically simulated using Unsteady-Reynolds-Averaged Navier-Stokes (URANS) and multiple Detached Eddy Simulation (DES) solvers: the Delayed-DES (DDES) and the Improved-DDES (IDDES). Two- and three-dimensional simulations are performed for each solver, and results are compared against experimental measurements in the literature. Results showed that three-dimensional simulations surpass two-dimensional ones in capturing the stages of dynamic stall and predicting the lift coefficient values, with a distinguished performance of the DES solvers over the URANS ones. For instance, the IDDES simulations, as an inherently three-dimensional solver, predicted the necessary cascaded amalgamation process of vortices to form the adequate strength of the dynamic stall vortex. This vortex size and timing provided accurate and sufficient suction that resulted in identical matching of the numerical and experimental lift coefficients at the peak value. Hence, the hypothesis that dynamic stall has a three-dimensional nature is supported by the superiority of the three-dimensional simulation in all aspects. In conclusion, it is found that dynamic stall is intrinsically a three-dimensional phenomenon.

I. INTRODUCTION

Dynamic stall phenomenon typically occurs when an airfoil rapidly changes its angle of attack near the static stall angle[1,2]. The phenomenon is characterized by a massive flow separation followed by reattachment at different stages of the cycle. The different stages of dynamic stall are shown in fig. 1 schematic drawing in chronological order. The phenomenon has been extensively studied in literature over the past few decades from the early efforts of McCroskey, Carr, and McAlister[2–5] to the recent efforts of Visbal[1,6,7] and Ansell[8]; and many studies reported the possibility of lift modeling and enhancement by exploiting dynamic stall[9,10]. Also, the phenomenon is widely present in many applications, such as helicopters[11], wind turbines[12], energy harvesting[13,14] and high speed flow applications[15].

Many experimental studies[2,3,5,8,16] investigated the effect of Reynolds number (Re) on the development of dynamic stall; in particular, a recent study[17] at a moderate Re of 1.35×10^5 will be used for validation in this article. The dynamic stall maneuver considered in the experimental study by Lee and Gerontakos [17] was numerically simulated by several researchers[18–21] and surprisingly, none of these numerical studies were able to replicate the experimental results. The main objective of this paper is to show that a proper numerical simulation of dynamic stall must be performed in three dimensions with an emphasis on capturing turbulent scales. That is, even though the studied body is an infinite-span, two-dimensional airfoil, the flow physics are inherently three-dimensional; i.e., dynamic stall is a 3D phenomenon.

A simple yet complete comprehensive description of dynamic stall development is given by Benton and Visbal[22]. The first feature, along the upstroke, is the creation of a Laminar Separation Bubble (LSB)[3,4] near the airfoil Leading Edge (LE). Meanwhile, there is a flow reversal at the Trailing Edge (TE), where a turbulent boundary layer starts propagating upstream of the airfoil. Then the LSB and the turbulent boundary layer interact with each other to create the Dynamic Stall Vortex (DSV) in a complicated process. Mulleners and Raffel [16,23] provided a detailed description of the DSV creation based on their experimental study. In particular, when the reversed flow reaches the LSB, the LSB bursts and creates a Leading Edge Vortex (LEV)[24]. Simultaneously, the rear separated turbulent flow evolves into a Turbulent Separated Vortex (TSV) located above the airfoil. Then, both the LEV and the TSV consolidate and form the DSV that convects over the airfoil upper surface. This dynamics is presented in a recent numerical study by Visbal and Garmann [1] and Visbal [6], in which Wall Resolved Large Eddy Simulation (WRLES)[25] is utilized as a high-fidelity numerical tool to capture such a rich dynamics. They concluded that complex separations and turbulent boundary layer interactions necessitate a high-fidelity simulation tool to be correctly predicted, where on the contrary, lower order models (e.g., averaging techniques) might not capture important physical aspects.

In this study, different turbulence models and numerical simulation techniques are used to demonstrate the three-dimensional nature of the dynamic stall phenomenon. The list includes the Reynolds-Averaged Navier-Stokes (RANS) and its unsteady version URANS, the DES and its following enhanced versions, the DDES and IDDES. The averaging techniques of RANS and URANS rely mainly on turbulence closure models[26,27] leading to questionable results when simulating flows with massive separations, which is the case for dynamic stall. Their main drawback stems from the fact that they average turbulent scales instead of resolving them. For example, these solvers can not accurately predict the exact static lift curve of an airfoil beyond the stall angle[28–30]. Another approach that is, though more expensive, capable of resolving

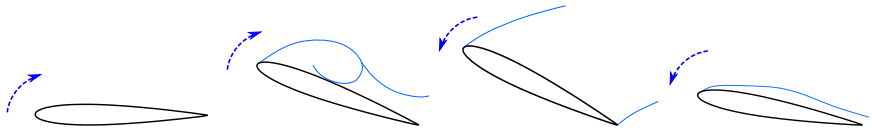

FIG. 1: Dynamic stall stages: (1) attached flow at lower angles of attack (upstroke), (2) dynamic stall vortex creation and convection above the airfoil (upstroke), (3) complete stall when the DSV sheds into the wake (downstroke) and (4) flow reattachment (downstroke)

the large (usually the most important) scales of turbulence is the Large Eddy Simulation (LES)[31]. In the LES approach, the large turbulent scales are resolved through a spatial filter, and tiny scales that are washed out by the filter are modeled by an ad-hoc model; they are called Sub-Grid-Scales (SGS). Interestingly, even with SGS modeling, the LES technique holds its position as the second most computationally expensive technique after Direct Numerical Simulations (DNS). The expensive requirements for outer flows are mostly demanded inside the boundary layer viscous sub-layer[32], where the no-slip boundary condition is satisfied and severe shear stress occurs. In contrast, for free shear layers and mixing ones, the LES technique is quite feasible. So, to mitigate the LES computationally expensive requirements near the wall, the Detached Eddy Simulation (DES)[28,33–36] was introduced as a hybrid RANS/LES solver.

The main idea behind the DES is to utilize each technique from RANS and LES where it serves the best: RANS near the wall where turbulent scales are much smaller than grid spacing, and LES in free shear layers away from the body where resolved turbulent scales are of the same order as local mesh size. Since the LES solution is not sensitive to SGS modeling away from the wall (i.e., in free shear layers), the RANS turbulence model could serve as the SGS for the LES; and this is the artifice that enabled this hybrid solver[28,33,37]. Then, the dual role of the solver is controlled by a switch that relies on grid spacing relative to the RANS length scale L_t. For example, the RANS length scale for k-ω turbulence model is defined as $L_t = k_t^{1.5}/\epsilon$, where k_t is the turbulent kinetic energy and ϵ is its rate of dissipation. In other words, if the mesh is locally fine for LES then it will be activated; if not, then RANS will be the choice. This formulation is the first version of the DES; it is called DES97 as conceived by Spalart [28].

In DES simulations, RANS is responsible for modeling the entirety of the boundary layer consisting of: the viscous sub-layer, log-layer and the outer layer[38]. It turns out that this version of DES has a serious drawback; the limiter (switch) is freely implemented all over the domain, which may be problematic in the regions where the mesh size is very fine in an attached boundary layer. In this case, the LES will be activated and take the role out of the RANS solver while the mesh is not fine enough for feasible LES simulation. This scenario results in a smaller eddy viscosity in the boundary layer, which leads to fictitious separation, named by Menter and Kuntz [39] as Grid-Induced Separation (GIS). As a remedy, the DES97 was upgraded by Spalart *et al.* [40] to the Delayed-DES. An extra shielding function was introduced to protect the RANS boundary layer region from getting usurped by the LES. The DDES adopts the same DES philosophy in resolving the flow: RANS is responsible for modeling all the boundary sub-layers and LES takes responsibility in free shear layer regions (i.e., outer flows). Unfortunately, the DDES suffers from a drawback in the boundary layer region despite of the shielding function. The DDES results can not match the universal log-layer law inside the boundary layer, especially for highly separated flows and turbulent boundary layers—a phenomenon known in the literature as "*log-layer mismatch*".

A new formulation was proposed by Spalart, Shur and others[41–43] to overcome the mismatch predicament by allowing the LES solution to penetrate more - correctly - in the turbulent boundary layer regions. In this formulation, instead of relying on RANS completely inside the boundary layer, the Wall Modeling LES (WMLES) is utilized to resolve the outer and log layers, which compose around 80 % of the boundary layer; while the viscous sub-layer is still being modeled by RANS. Also, the interface between RANS and WMLES solvers is not dictated by the limiter value and the grid size (i.e., user defined) any more. Rather, it depends on the grid and/or the solution itself, so it can not be specified directly by the user. This formulation is referred to as the Improved-DDES[41–43]. The reader is referred to Larsson *et al.* [25] for more details about WMLES and its implementation, and to Spalart [44], Mockett [45] for information about different variants of DES solvers. In terms of RANS modeling, all of the previously mentioned solvers could utilize the Spalart and Allmaras [46] (S-A) closure model directly or the k-ω SST model[47,48] that is altered for DES integration by Travin *et al.* [49] and Gritskevich *et al.* [50]. In the current study, the k-ω SST is favored over the S-A model because it can handle severe pressure gradients in the boundary layer and being a complete two-equation turbulence model[26,27].

Computational simulations of dynamic stall have been performed in numerous studies, and it is out of the scope of this work to provide a comprehensive discussion of these efforts. However, it may be prudent to discuss some relevant efforts. Martinat *et al.* [51] employed URANS and DDES with different turbulence models to reconstruct McAlister, Carr, and McCroskey [52] experimental study results. The simulations were performed for 2D and 3D domains. Results from both simulations did not perfectly match the experimental lift coefficient data from McAlister, Carr, and McCroskey [52]. However, the DDES simulations results were in a better agreement with the experimental data than URANS; and the 3D ones had even a better behavior over all. Wang *et al.* [18] performed 2D

URANS simulations of Lee and Gerontakos [17] experimental dynamic stall maneuver; they compared different turbulence closure models. The numerical results were in agreement with the experimental lift coefficient values within the upstroke, while it failed to match the downstroke values. In a following study, Wang *et al.* [19] performed URANS simulations with more advanced turbulence closure models in addition to DDES simulations; both simulations were performed for 2D and 3D domains. The results predicted the maximum lift coefficient using 2D URANS simulation, but it did not correctly capture the downstroke loads. Their 3D simulations were attempted based on the findings of Martinat *et al.* [51], but interestingly, the obtained lift values of the 3D simulation mismatched the experimental measurements, even more than the 2D ones. Similar 2D DDES simulations were performed by Wang *et al.* [19] and Singh and Páscoa [21]. The latter[21] performed DES and URANS simulations over a 2D mesh for the dynamic stall maneuver of Lee and Gerontakos [17]. As may be expected, they were able to predict the upstroke correctly but failed to capture the maximum lift coefficient. Also the resulting values during the downstroke did not match the experimental measurements. However, more information about the flow field was presented in their work; they provided a comparison of the wake velocities at a unit chord downstream of the airfoil with experimental measurements. This comparison showed that in contrast to all performed URANS simulations, the DDES results nearly matched the experimental wake measurements. Finally, Gharali and Johnson [20] performed a 2D URANS simulations relying on a grid crafted with extra care and precision. They were able to predict the lift curve slope efficiently, achieve good matching with the lift peak value and the downstroke lift, of course within the limitations of RANS. This finding highlights that mesh considerations is an important factor for simulations of complex flow fields even when using the less demanding URANS, let alone the DES family of simulations. As a consequence, a meticulous approach and consideration for mesh generation is adopted in the current study especially for the LES part as will be shown later.

The above simulations point to the importance of a 3D simulation for proper capturing the rich flow physics in dynamic stall. The main objective of this paper is to test this specific hypothesis of the 3D nature of dynamic stall and point out the prominent role of the TSV and its interaction with the LEV during the dynamic stall process. The investigation is carried out utilizing different simulation techniques URANS, DDES and IDDES, comparing their results with the experimental data of Lee and Gerontakos [17]. The numerical setup and the settings of each solver along with validation for simulations are discussed in section II. Then, the dynamic stall simulation results using each technique are presented in section III. Next, a detailed discussion of the dynamic stall stages and the ability of each solver to capture its dynamics is presented in section IV, followed by discussion and conclusion.

II. NUMERICAL SETUP

Simulations were performed for the NACA 0012 airfoil pitching around the quarter-chord point at Reynolds number $Re = 1.35 \times 10^5$ and reduced frequency $k = \omega c/2u_\infty = 0.1$ (where c and u_∞ are the chord length and free stream velocity, respectively, and ω is the motion frequency) matching the dynamic stall maneuver of the experiment by Lee and Gerontakos [17]. The pitching motion is defined as:

$$\alpha(t) = \alpha_m + \alpha_o \sin(\omega t), \tag{1}$$

where α_m is the mean angle of attack set at 10°, α_o is the pitching amplitude set at 15°, and ω is selected corresponding to $k = 0.1$. The numerical simulations and grids generation were performed using Ansys Fluent 19.2 and ICEM CFD 19.2 software, respectively, while the motion was implemented by a User Defined Function (UDF) in Fluent. All the simulations were carried out on the "HPC" cluster computer available at the University of California, Irvine. The grid generation and case setup will adopt most of the information available in the previous study by the authors[53].

A. Grid

At first, a 2D mesh was generated, then extruded to create a 3D mesh. The resulting mesh was used for both URANS and DES simulations. The surface mesh was crafted with extra precautions and high quality for proper 3D DES simulation. Even though the superior requirements are needed for DES simulations, the RANS solver could be performed with most grid types without stringent requirements. Also, the RANS could handle different types of grids with different discretization schemes, which is not the case for an LES solver. So, the mesh was crafted having in mind the DES simulations and relying on the fact that whatever suites DES will surely be convenient for RANS too. The mesh was divided into two different zones as shown in fig. 2a: a static outer shell zone with the inlet and outlet surfaces, and a rigid rotating zone enclosing the airfoil with an interface between these two zones. This division of the mesh domain was adopted to accommodate the airfoil rotation. The interface was set to be far away from the airfoil to ensure that it will not interfere with the LES portion of the solution.

The mesh size in an LES simulation is critical because it resembles the spacial filter of the solution, hence defining the resolved spectrum of turbulence scales. It could be thought of as the analogue of the sampling frequency for any temporal transformation. However, the spatial filter comes with its complication: instead of being implemented in one dimension similar to the temporal case with Δt, it is a multi-dimensional transformation that is performed for the three dimensions $(\Delta X, \Delta Y, \Delta Z)$ simultaneously. Hence, the grid size should be selected comparably taking into account the interplay between these dimensions. Consequently, if the grid size (i.e., spatial sampling) is very fine in one direction compared to the other two, it may be futile for the LES solver. Moreover, in

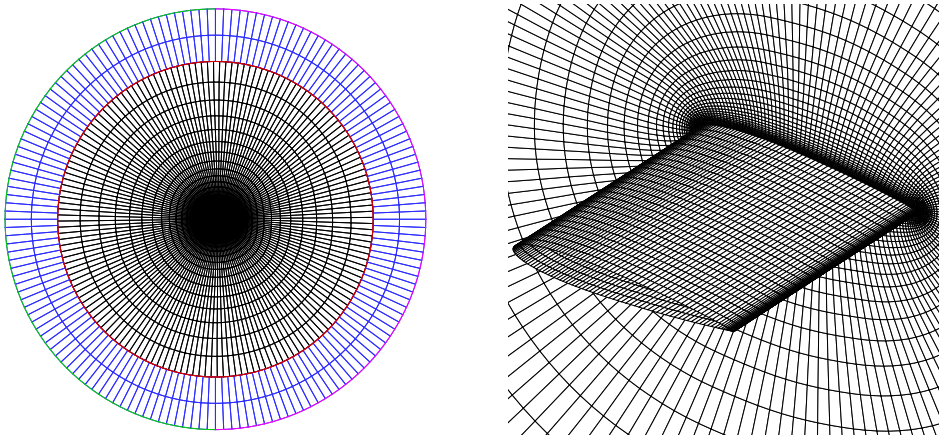

(a) (b)

FIG. 2: Different mesh representations: (a) 2D section showing different zones: rotating one in black, static outer shell in blue, interface surface in red, inlet in green and outlet in magenta; (b) 3D view showing element distribution.

contrast to temporal filtration (or discretization), finer meshes do not always result in better simulations[35], which implies that one can not perform a grid refinement study for LES to reach a "*grid independent solution*" as typically done with RANS solvers[35]. This situation also holds for the time step in LES simulations. Therefore, a grid independence study was only performed for RANS simulations in this article.

Another important aspect in generating the mesh is the resolution of wake mixing layers—a layer where flow separates from the body and multi turbulent scales are generated due to mixing. This phenomenon is generalized and defined by Menter[54] as the Separating Shear Layer (SSL); it has to be resolved by the LES solver. Recall that, because of the DES hybrid nature, the RANS is activated inside highly viscous boundary layer regions and LES inside the free shear layer. The mixing scales in the SSL demand a finer mesh in this region for LES to be activated and resolve them correctly. Otherwise, the DES limiter defined by the grid spacing will allow the RANS solver to handle this part of the wake, which will damp most of the vortical structures in this region. So, for proper LES resolution, extra mesh refinement is needed for the region where the SSL occurs (i.e., near the TE). However, this extra refinement near the TE is closely tied to the previous discussion of selecting the mesh sizes in different directions. For example, if a very fine planar mesh is adopted but with a large spanwise spacing, then this extra refinement will be fruitless and the DES limiter will still activate the RANS solver based on the coarser mesh size. On the other hand, if the mesh is refined equally in all the directions, then the LES could be activated near a boundary layer region and induces a GIS if the local mesh size is not adequate for proper LES boundary layer resolution. This discussion shows the importance of mesh size selection for different regions in the simulation and the benefit of DDES shielding function protecting the RANS boundary layer solution from unworthy intervention by the LES solver.

As for the mesh type, it was shown by Kozelkov *et al.*[55] that unstructured meshes used for performing DES simulations require more elements to reach the same solution of a structured mesh. The study showed that unstructured-polyhedral meshes required two to three times more elements than a block-structured-hexahedral mesh, and it could be six times for the tetrahedral ones. The unstructured meshes are applicable for DES and DDES, but not so convenient for IDDES because the WMLES is far from being implemented on an unstructured grid[42]. Hence, a multi-block-structured mesh was used for the current study. The mesh topology is an O-grid over a rounded TE airfoil; the TE is rounded to facilitate the use of the O-topology. The 2D planar mesh was composed of quadrilateral elements and the 3D one was generated from hexahedral ones as shown in fig. 2. The number of elements and their distribution over the domain were selected following the guidelines by Spalart and Streett[56] and the DES NACA 0012 grid implemented by Shur *et al.*[33]. The dispersion of elements takes into account the different regions in the mesh, such as viscous, focus and departure regions[56].

The main requirement by RANS solver (k-ω turbulence model) is the first cell height at the boundary layer treatment near the wall. It was estimated based on Schlichting's skin friction formula[32] to have a non-dimensional wall-distance y^+ less than or equal to unity. Then an extra one fourth reduction for the first cell height was applied to compensate for the airfoil dynamic motion, resulting in a final value of $h = 1.1 \times 10^{-4} c$. The boundary layer treatment consists of 30 layers with a slower expansion rate than what is required by a regular RANS simulations; as recommended by Shur *et al.*[33]. The slower expansion rate selection allowed the boundary layer

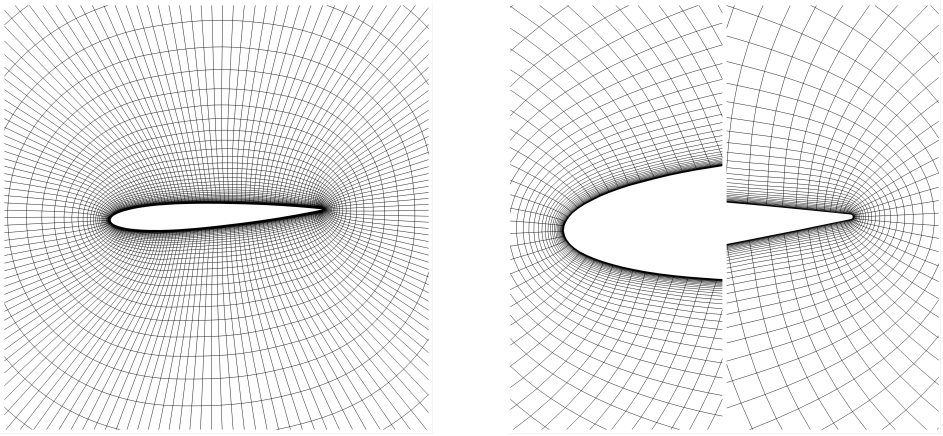

(a) (b)

FIG. 3: Different mesh domains: (a) Growth rate and spacing near airfoil wall; (b) Treatments of leading and trailing edges.

mesh treatment to penetrate more in the flow regions where severe viscous stresses are not present (i.e., outside the boundary layer). Moreover, the increased number of layers along with the expansion rate will be utilized by the WMLES in the IDDES simulations. The small expansion ratio is essential for LES solvers because these solvers are very sensitive to sudden length changes. Another aspect considered while meshing was the special attention given for the TE region to overcome the SSL predicament discussed before.

The spanwise width is selected based on the recommendation by Shur *et al.*[33]. They mentioned in their study that $1c$ is sufficient to capture the flow field features for a streamlined body at high, but still moderate, angles of attack. Moreover, they mentioned the study by Najjar and Vanka[57] where a $2\pi c$ spanwise width domain was selected to predict the drag over a normal flat plate, which is considered as a bluff body. Even though Najjar and Vanka[57] mentioned in their study that the 2π period is several times larger than the distance between two consecutive streamwise ribs, they utilized this thickness to make sure they are capturing dynamics in the spanwise direction. Travin *et al.*[35] used $1D$ spanwise width while performing their seminal DDES simulation over a cylinder. They reported that there were no considerable differences between cases that adopted πD, $2D$ or even more. In a recent study of dynamic stall onset by Benton and Visbal[22] they selected the spanwise width to be $0.05c$ aligning with the recommendation of Menter[54], as long as the periodic boundary condition is selected for the domain sides. In fact, this boundary condition is the crucial point for mimicking an infinite airfoil in a computational domain. The spanwise width selection is sufficient as long as periodic boundary conditions are adopted and the spanwise domain extends to two consecutive streamwise ribs, which is evident in fig. 6b from our $1c$ selection. The spanwise spacing was selected based on the non-dimensional wall distance z^+ in z-direction with a 25 equally spaced elements over the one chord length. All these aspects are implemented in a $20c$ radius ($15c$ for the rotating part and $5c$ for the outer shell) mesh with 160 elements over the airfoil and 62 normal to its surface, resulting in a total of 2.48×10^5 elements with the origin placed at the quarter chord, as shown in fig. 3.

B. Solver Settings

The pressure based solver was adopted for all simulations since the flow is incompressible; and all simulations were transient in time. URANS, DDES and IDDES simulations shared the same case setup unless stated otherwise. Incompressible air was selected as the material for all mesh zones and a UDF was constructed to define the inner-rigid-rotating-zone motion, while the outer shell zone remained static. The boundary condition for the airfoil surface was set to non-slipping wall. The inlet semi-circle surface was set to velocity inlet with turbulence intensity and length scale equal to 5% and 10%c, respectively. The inlet intensity was selected based on an assumed fully turbulent flow[26]. The outlet surface was selected as an outflow rather than constant pressure. The reason behind this selection is that outflow, in contrast to constant pressure, allows for vortices to cross the boundary. Otherwise, the constant pressure boundary condition will damp the vortical structures along with their accompanied pressure gradients while convecting through the boundary. The boundary conditions for the two bounding side walls were set as translational periodic. This choice allowed turbulent structures to be resolved when they are in contact with the boundaries[54]; other boundary conditions such as symmetry (i.e., slip-wall) may result in nonphysical constraints over the resolved turbulent scales. Also, the selection of periodic condition allows for

flux convection through the boundary, which is essential for simulating an infinite spanwise domain.

The coupled scheme was used for pressure velocity coupling and the under relaxation factors were set to unity. Least Squares Cell method was selected for spatial gradient discretization. The pressure and turbulence discretization were selected as standard and second order upwind schemes, respectively. Then the case setup was left with the most important discretization, especially for LES solver, which is the momentum scheme. The second order upwind scheme was selected for URANS simulations, however, this type of schemes are too dissipative when used along with LES solvers. So, differencing schemes are preferred for the LES solver, though with some limitations. The regular central differencing scheme can introduce nonphysical wiggles in the flow, so the bounded central difference scheme for momentum discretization[54] was used instead.

As for temporal discretization, the bounded second-order-implicit-dual-time stepping integration was used with 10 iterations for the inner loop. The best guess in DES simulations for time step is to have unity Courant–Friedrichs–Lewy (CFL) number $\approx 1 = u\Delta t/\Delta x$ at the LES region[54]. For URANS, however, an appropriate time step criterion is to ensure a balanced choice: the time step must be large enough for proper averaging of turbulent structures and small enough for proper discretization of the motion time constant. The maximum velocity u_{max} in the LES region is estimated to vary from $1.2 - 1.5 \times u_\infty$[56]. Hence, to satisfy the CFL criterion, the time step will have to be smaller than $\Delta t = \Delta_{max}/u_{max}$, where Δ_{max} is the grid size in the LES portion (i.e., focus region) corresponding to the spanwise mesh spacing ΔZ. As such, the time step was set to $\Delta t = 0.015\ s$ for all simulations, resulting in 1062 time steps per one pitching cycle. Finally, for the case setup, the URANS simulations were initialized using hybrid initialization while the DDES and IDDES were initialized with a previously converged URANS solution.

C. Solution Assessment

To assure convergence, residuals were monitored and checked for stable behavior, but they were not used as a convergence criterion. Instead, the lift coefficient time history was examined to decide convergence. For example, while simulating static airfoil, convergence was assumed when the C_L reaches a constant value. On the other hand, for oscillating airfoils, convergence was considered when the lift coefficient reaches a periodic solution after performing 15 complete cycles for the URANS simulations and 25 cycles for DES. Another criterion, dedicated especially for proper turbulence modeling, is the non-dimensional wall distance y^+ values. In both URANS and DES simulations, the y^+ values were assured to be less than unity. The inlet and outlet mass flux difference was checked to be less than 10^{-8} for adequate continuity convergence. As mentioned before, the CFL values should be around unity for LES simulations. So, the LES portion in the solution was first identified, then the CFL values were checked within it. To set apart the LES from the RANS region, one can rely on the"*DES Turbulent Kinetic Energy Dissipation Multiplier*" value; if it is less than unity, then it indicates a RANS region and LES otherwise, as shown in fig. 4a. Accordingly, the CFL values could be seen to be in the acceptable range for the LES region, as shown in fig. 4b.

D. Validation

A crucial task in the validation process for URANS simulations is to reach a grid-independent solution— a feature that is not applicable for IDDES and DDES simulations, as mentioned before. Two-dimensional URANS simulations were performed for a static airfoil at 10° and 30° angles of attack. The grid independence study included two step mesh refinements, and details are listed in table I. Relative error in the lift coefficient was computed between each refinement step, and the study showed relative error values less than 1%. Moreover, for both simulations, the numerical C_L values matches the experimental data. Hence, the first coarser mesh was selected to be used for the rest of the simulations. Another series of 2D URANS simulations were performed to construct the 2D static C_L-α curve. The resulting curve was validated against the experimental data of Lee and Gerontakos[17]. It is clear from fig. 5a that the 2D URANS lift coefficient values are in fair agreement with the experimental data. On the other hand, for DES simulations, since the concept of grid-independent solution is not always viable, validation was conducted only against experimental data. Moreover, the grid and time step sizes are made sure to follow the guidelines presented by Cummings, Morton, and McDaniel[59] and implemented for a DDES simulation by Qin *et al.*[60]. A series of 3D IDDES simulations for static airfoil beyond the stall angle (where the lift coefficient does not depend on the Reynolds number) were performed. Results were compared in fig. 5b with respect to experimental data from Critzos, Heyson, and Boswinkle Jr[58] and DES97 numerical simulations from Shur *et al.*[33], in which the comparison shows excellent agreement.

TABLE I: Information of grid study and lift coefficient values.

Grid		Coarse	Medium	Fine
No. of Nodes		9600	38080	151680
C_L	10°	0.89	0.9	0.9
	30°	1.205	1.236	1.241

III. RESULTS

This section presents the obtained results from the performed simulations using different solvers. First, an overview of the capabilities of URANS and hybrid solvers are discussed, while highlighting the limitations and strengths in resolving the features of the flow field features. Second, the resulting lift coefficient values from URANS and DES (i.e., DDES and

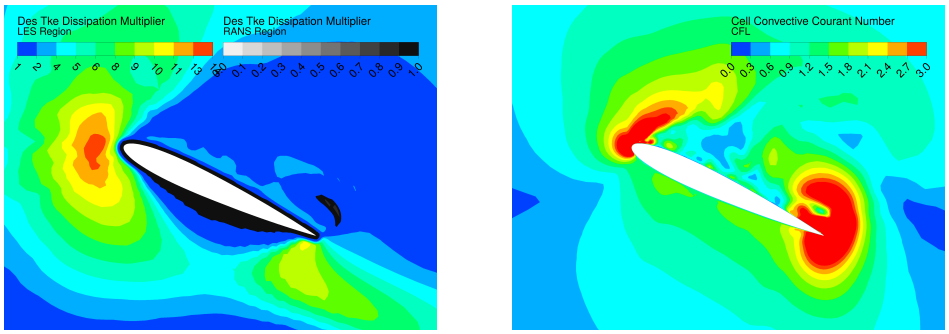

(a) (b)

FIG. 4: Mid-plane contour plots for the IDDES simulation at $t = T/4$: (a) DES Tke Multiplier contour values, where RANS and LES domains are distinguished by color; (b) various CFL contours.

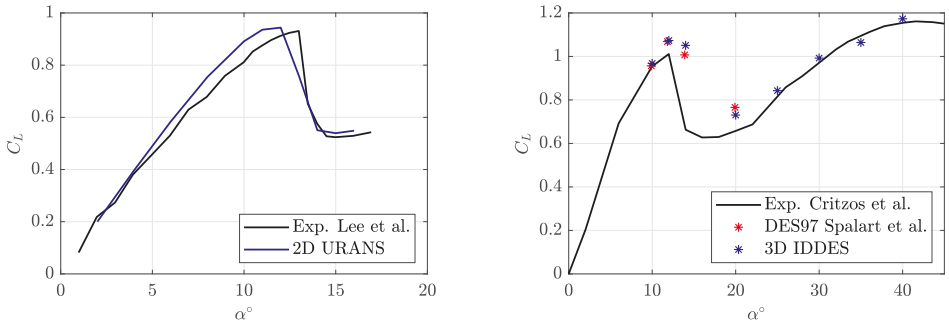

(a) (b)

FIG. 5: Different plots used for validation: (a) 2D URANS static airfoil results validated against experimental data; (b) 3D IDDES simulation lift coefficient values at selected angles of attack versus experimental data[58] and DES97[33] results.

IDDES) simulations are compared against each other; the comparison is performed in terms of each solver ability to capture various stages of dynamic stall. As anticipated, the comparison will reveal the superior behavior of 3D models over 2D ones.

A. Evaluation of Solvers Results

A qualitative assessment of each solver can be made by inspecting different flow visualizations, as shown in fig. 6. Q-criterion iso-surfaces[61] (i.e., representation of the vortices boundaries) resulting from 3D IDDES and URANS simulations at the same time instant are presented in figs. 6a and 6b (Multimedia available online), respectively. These iso-surfaces are filled with velocity magnitude to provide a picture of the underlying flow field. It is clearly seen that IDDES simulation results in a rich three-dimensional vortical structure than the URANS solution. In fact, the Q-criterion iso-surfaces for the 3D URANS could be thought of as the 2D URANS planar z-vorticity boundary extruded in spanwise direction, as shown in figs. 6c and 6d. Inspecting fig. 6a in more detail, the presence of LE separation, which rolls up and creates a LEV, is clearly evident; this LE separation is the main foundation for predicting the DSV within the URANS framework. Also, no turbulent separation of any scale is present over the airfoil upper surface, which restricts the URANS solver from predicting the amalgamation of these turbulent eddies into the TSV. As such, the interaction between the LEV and TSV is unavailable for URANS solver. On the other hand, a notable turbulent separation over the airfoil upper surface occurs in the IDDES simulations, as shown in fig. 6b. As will be discussed later, these resolved scales and their mutual interactions are essential for accurate prediction of the lift coefficient throughout the dynamic stall cycle, especially the lift peak value and its timing.

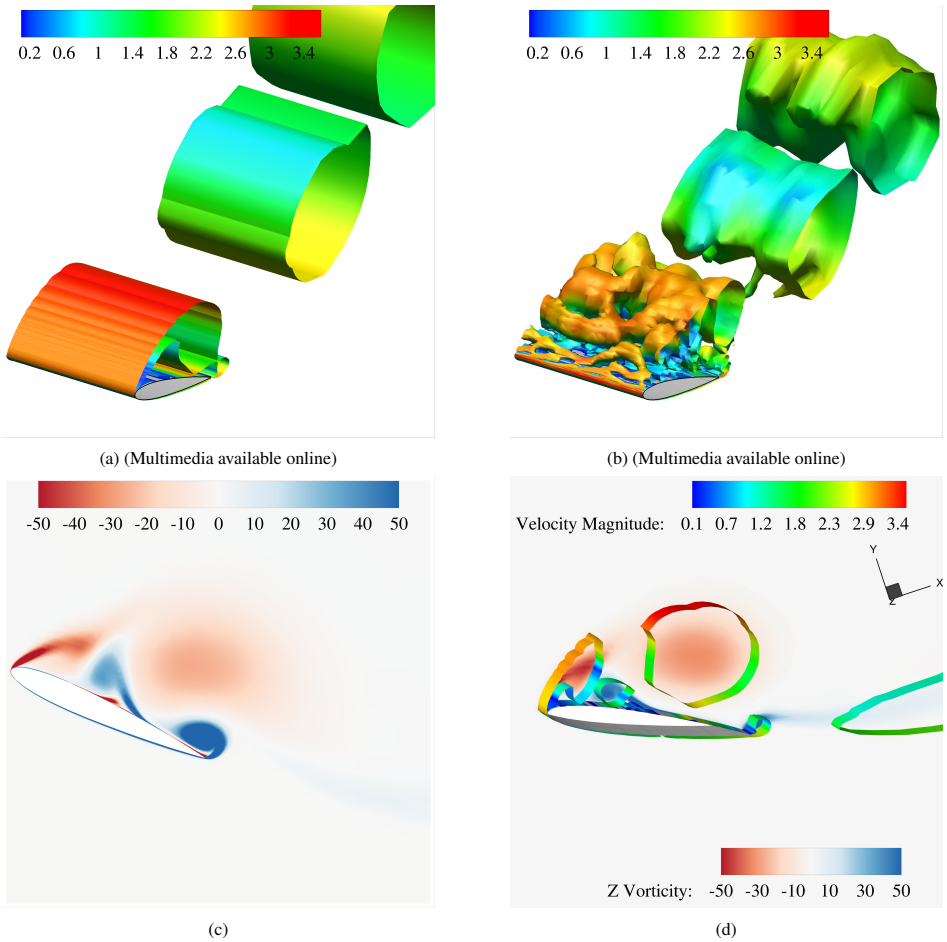

FIG. 6: Different CFD visualizations used for comparison: (a) 3D URANS Q-criterion iso-surfaces at $Q = 0.5s^{-2}$ flooded with velocity magnitude at $t/T = 1/3$; (b) 3D IDDES Q-criterion iso-surfaces at $Q = 0.5s^{-2}$ flooded with velocity magnitude at $t/T = 1/3$; (c) 2D URANS vorticity contours at $t/T = 0.21$; (d) 3D URANS mid-plane z vorticity and Q-criterion iso-surface at $Q = 0.5s^{-2}$ flooded with velocity magnitude at $t/T = 0.21$.

The time histories of the lift coefficient over the last five simulated cycles from 2D, 3D URANS and IDDES are presented in fig. 7. The 2D and 3D URANS results are perfectly repeatable to an extent that each cycle plot is indistinguishable from the another. This perfectly coherent behavior indicates the lack of capturing chaotic turbulent scales by URANS (i.e., damping the rich turbulence dynamics by averaging). On the other hand, 2D IDDES results are not repeatable (i.e., coherent) when compared with URANS as shown in fig. 7a. However, the comparison demonstrates that 2D IDDES simulations are uncertain in predicting repeatable lift coefficient values, resulting in erroneous behavior of the lift coefficient. In particular, the downstroke values experience significant fluctuations and deviations from the experimental results. Nevertheless, there is a reasonable match with the experimental data in the upstroke, because the flow is seamlessly attached to the airfoil, where the 2D DES family of solvers could provide reliable results[33]. So, the 2D IDDES simulations will be discarded from the ensuing discussions. In contrast to the 2D IDDES, the resulting lift curve from 2D URANS presented in fig. 7a,

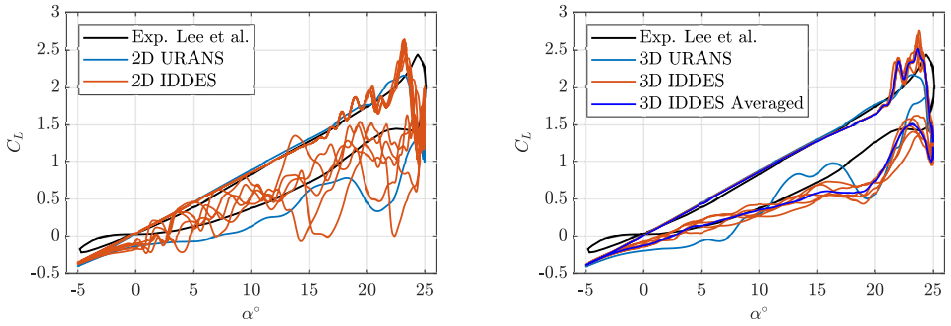

FIG. 7: The lift coefficient values for the last five cycles of different solvers compared with experimental data (a) 2D URANS and IDDES; (b) 3D URANS, IDDES and the ensemble average for the IDDES lift coefficient.

highlights a reasonable behavior following the experimental data during the downstroke and a perfect matching during the upstroke until 22°, at which the 2D URANS fails to predict the lift coefficient correctly.

Comparison of the 3D simulations is presented in fig. 7b. It is evident that 3D URANS lift coefficient has an almost perfect alignment with experimental data during upstroke, except for the peak value, inheriting this drawback from its 2D version. During downstroke, the 3D URANS results lead to a substantial enhancement in the lift coefficient over the 2D ones where it is able to match most of the experimental behavior in the downstroke, especially after the initial reattachment takes place (i.e., 18° ↓). However, the 3D URANS results mismatch the experimental data at the beginning of the downstroke where there is a kink in the lift coefficient around 22° angles of attack, as shown in fig. 7b. In contrast, the 3D IDDES results demonstrate better correspondence with experimental data compared to other methods. It is not perfectly repeatable as 3D URANS, which is expected, because of the chaotic turbulence structures that are resolved by the LES solver. But the differences between the presented five cycles are within limited deviation from the computed ensemble averaged value, which indicates that different cycles are closely correlated to each other. The 3D IDDES results match the experimental values for most of the upstroke cycle and accurately predict the lift coefficient peak value—a strength that other solvers lacked. Moreover, the 3D IDDES results aligns with the experimental data at the beginning of the downstroke, and the kink of the lift coefficient is captured. However, it then deviates from experimental data till it perfectly matches it again near the end of the cycle. It is worthy to mention that DDES simulations were also performed for this dynamic stall maneuver, however, the results are not discussed at this section because they share the same characteristics as the IDDES. Most of these observations emphasize that the dynamic stall phenomenon should be considered as a highly separated flow problem that possesses a 3D nature, which demands a high-fidelity scale-resolving simulation tool for proper modeling and analysis.

B. Comparison of the Lift Dynamics

In this section, a detailed discussion about the lift dynamics resulting form each solver is presented in comparison to the experimental findings[17] and the flow physics discussed in recent literature[1,6,22]. In particular, we will assess the ability of each solver to capture different stages in the dynamic stall phenomenon. To properly do such an assessment, we will first present a demonstration of the different stages in a dynamic stall cycle relying on the experimental results of Lee and Gerontakos [17].

At early stage of a typical dynamic stall cycle, the airfoil is pitching up at relatively small angles of attack leading to an attached flow; and the lift curve slope is fairly constant, as shown in fig. 8. After instant (i), the airfoil continues to pitch up while experiencing a TE flow reversal over the suction surface. The flow reversal constitutes an unsteady turbulent boundary layer that propagates upstream as the airfoil pitches more. Simultaneously, a LSB is created at the LE and a turbulent separated layer is formed near the TE. Also, there is a shear layer emanating from the LE that feeds both the LSB and the TE turbulent separated layer with vorticity. Up to this moment (ii), the flow still has no severe separations, and the lift curve slope C_{L_α} is approximately equal to the airfoil static lift curve slope value. At the end of the flow reversal stage, the backward flow that was propagating ahead towards the LE is about to collide with the LSB. When the collision takes place, the LSB bursts to form a LEV. Meanwhile, near the trailing edge, the turbulent separated layer has grown and covered the majority of the airfoil upper surface, while forming small eddies. These eddies, in turn, amalgamate in a more coherent structure, referred to as the TSV. Then, the LEV continues to grow while being fed by the LE shear layer, until it is strong enough to pull the TSV towards it. They then both roll up

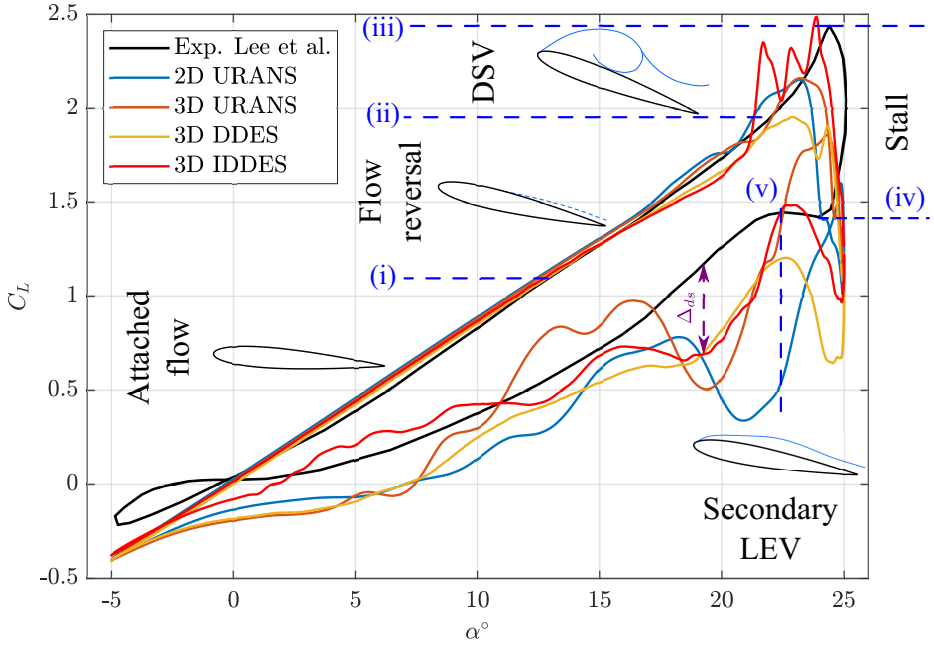

FIG. 8: A comparison between different solvers lift coefficient values and experimental data.

together creating the DSV, which convects over the airfoil upper surface till it sheds away. During the DSV creation and convention stage (ii)-(iii), the lift coefficient reaches its maximum value and its slope increases significantly.

Momentarily after the DSV sheds away causing a sudden loss in lift values, the stall stage (iii)-(iv) begins, where the airfoil operates in a massively separated flow and the lift values drop dramatically. After this stage, the downstroke starts, and the airfoil could be considered as if it were operating stationary in a massively separated flow. The LE separated shear layer is still in action and the turbulent eddies over the airfoil are still present. This dynamics, in turns, provides an opportunity for the creation of another vortex. Remarkably, a smaller LEV is created, noted as the "Secondary LEV" by Lee and Gerontakos [17] marked at instant (v) in fig. 8. It is important to mention that the Secondary LEV is not always present for every dynamic stall maneuver. A specific combination of Reynolds number, reduced frequency and airfoil kinematics is required for such phenomenon to occur, but for example, at higher reduced frequencies, there may not be a sufficient time for the Secondary LEV to form. In fact, even the DSV vortex and shedding is function in the pitch rate as presented in Fouda *et al.* [62] study. After the Secondary LEV stage, the airfoil airfoil pitches down more, and the flow starts to reattach till the end of the cycle.

The resulting C_L dynamics from each solver will be compared against the experimental data in the light of the previous discussion about different stages within a dynamic stall cycle. One cycle from each simulation is selected to facilitate the comparison. In fig. 8 five plots are presented: the experimental data, 2D URANS, 3D URANS, 3D DDES and 3D IDDES. Starting with the URANS simulations, it is clearly visible that both 2D and 3D simulations are able to capture most of the upstroke dynamics till $\alpha = 22^\circ$ when complex dynamics starts to evolve. Afterwards, they both fail to predict the lift peak value, which implies that the predicted DSV strength is not accurate compared to the experimental case. Although the peak value is not correct, both simulations are able to regenerate the sudden increase in the lift curve slope, which is of no surprise as they both captured the DSV though with an inaccurate strength. This failure is translated directly to a deviation of the lift curve from the experimental data at the stall region. Moreover, the 2D URANS fails to predict the Secondary LEV; there is no sign of it in the lift results. In contrast, the 3D URANS is able to capture the Secondary LEV, but neither the timing nor the strength are correct, resulting in an over estimation of the C_L values. During the rest of the downstroke, the 2D URANS results are not matching the experimental data, but the 3D ones show better behavior where they reasonably match the experimental data in the region $17^\circ - 12^\circ$. The fact that the 3D simulations achieve better results compared to the 2D ones even within the inaccurate URANS framework is one

of several evidences supporting the argument that dynamic stall is a 3D phenomenon, especially when massive separation occurs during the DSV creation and downstroke reattachment process.

It may be anticipated that DDES simulation results in a better agreement with experimental data than URANS since it is a hybrid RANS-LES solver, but it turned out not to be the case. In fact DDES underpredicted the DSV strength compared to both experiment and URANS, and it failed to follow the lift curve during the stall portion. Although it predicts a correct timing of the Secondary LEV, the estimated strength is not accurate. Moreover, the DDES downstroke results are not matching the experimental data. This poor behavior of the DDES solver in predicting the DSV strength and the Secondary LEV can be anticipated. Recall that the DDES is just DES97 with the RANS solution protected by the shielding function; there is no WMLES, the inherently three-dimensional solver, to resolve the mixing and buffer layers of the turbulent boundary layers. This formulation is actually the main reason behind its inferior performance: the communicated modeled turbulent structures by the RANS solver to the LES are not sufficient for LES to generate the TSV, because they lack the rich information generated by the WMLES capturing most of the turbulent boundary layer. So, there are no three-dimensional rich vortical structures resolved by the LES solver, despite being a three-dimensional simulation, yielding an underprediction of the DSV strength and the Secondary LEV. This conclusion serves as a second evidence to support the argument of the 3D nature of dynamic stall.

The IDDES simulation results are distinguished with the best performance. Unlike others, the IDDES is able to predict correct timing and strength for both the DSV and the Secondary LEV, which allowed it to match the experimental lift coefficient value at the peak point and the Secondary LEV. Moreover, the lift curve slope at the DSV stage (ii)-(iii) is almost perfectly matching the experimental data with some wiggles in the C_L values. This wiggly response is a natural result of the resolved vortical structures forming on the airfoil upper surface because of the present turbulent separation. The superior results of the IDDES are made possible because of the WMLES ability to capture the outer and log layers of the turbulent boundary layer over the airfoil. These turbulent structures are the ones that amalgamate into the TSV and interact with the LEV to form the DSV. Moreover, they play an important role in the creation of the Secondary LEV, where they interact with the LE separated shear layer and eventually transform into the Secondary LEV. Also, the IDDES achieved the best agreement with experimental results all over the cycle. It mainly failed to match the experimental data at two instants: after the Secondary LEV where the difference between simulations and data is marked as Δ_{ds}, and at stall. The mismatch at these two instants could be a result of the coarse mesh in the LES wake region that encounters the convected vortices, which in turns, does not allow the LES solver to hold the DSV and the Secondary LEV more as they are washed away. The superiority of the IDDES in predicting most of the features within a dynamic stall cycle can be considered as a third evidence for the 3D nature of dynamic stall. That is, not only three-dimensional simulations are needed for correct prediction, but also a solver that is capable of capturing the three-dimensional complex turbulent features of the flow is required for correct modeling.

The nearly perfect IDDES C_L values are compared with previously published numerical simulations mentioned in section I, as shown in fig. 9a. The comparison highlights the accuracy of the present simulation versus the past ones in comparison to the experimental data, which points to the meticulous approach adopted in this study for DES simulations, as discussed in section II. The lift coefficient values at the peak and the Secondary LEV instants are equal to the values from the benchmark study[17]. Moreover, the overall lift coefficient time histories are identically matching the benchmark study throughout 85% of the cycle; the 15% mismatched portion is at the downstroke from the Secondary LEV instant to 15°. Finally, a sensitivity study of time step and its effect on IDDES is presented in fig. 9b. The study was done for two different time steps $\Delta t = 0.012\ s$ and $0.018\ s$ different from the value used in the simulations throughout the paper ($\Delta t = 0.015\ s$). Interestingly, the resulting lift changes as a consequence of the change in the strength and timing of the Secondary LEV, but not significantly. Moreover, the downstroke reattachment process is not the same for all cases as present from the discrepancy in C_L values shown in fig. 9b. Although the downstroke results are altered, the maximum lift coefficient which depends on the DSV strength is still the same for all simulations, matching the experimental data. This time sensitivity study is presented to show that IDDES simulations are very sensitive towards time step selection, and a time independent solution is not well posed in hybrid solvers, similar to the grid dependency dilemma discussed before.

IV. DYNAMIC STALL DEVELOPMENT FOR DIFFERENT SOLVERS

A more elaborate discussion for the DSV creation process is presented in this section. Each solver is assessed with respect to its accuracy of capturing separation, vortex amalgamation, the DSV strength and convection dynamics. Unlike previous discussion where integral quantity (i.e., lift coefficient) was used, field quantities are considered in this analysis. The study will be pursued based on the mid-plane z-vorticity contours and flow streamtraces at fundamental instants of the dynamic stall phenomenon. Moreover, the instantaneous lift coefficient values along with the corresponding pressure coefficient will be presented for each vorticity frame (i.e., time snapshot).

First, a chronologically ordered frames of the mid-plane z-vorticity contours with the flow streamtraces are shown in fig. 10; each column represents a distinct solver. Clockwise vorticity is assumed to be negative and all the figures share the same contour levels. Second, the pressure coefficient corresponding to the selected frames is presented in fig. 11. To facilitate the comparison of the pressure coefficient at different snapshots, the pressure coefficient is shifted to have common vanishing value at the stagnation point (i.e., the point of maximum C_p value in the plot). Finally, a comparison of the lift

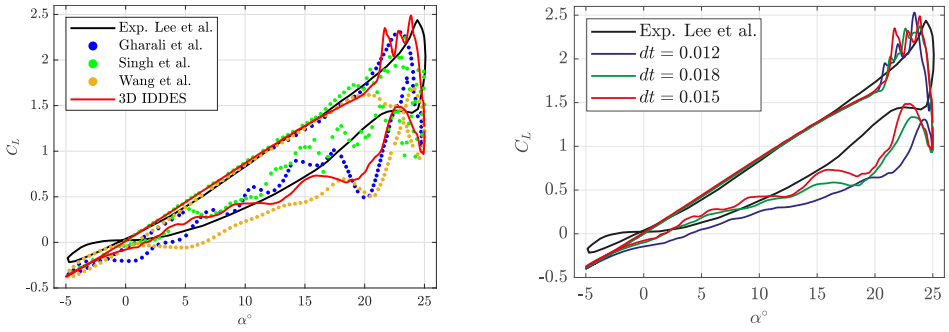

FIG. 9: (a) Current numerical IDDES simulation compared against the experimental data[17] and previous numerical efforts by Gharali and Johnson[20], Singh and Páscoa[21] and Wang *et al.*[19]; (b) Time step sensitivity results for the IDDES simulations.

coefficient time history versus the experimental one is presented in fig. 12, with a corresponding marker for each instant in fig. 10. The selected snapshots from each solver are considered to show the special instants corresponding to major flow field features (e.g., vortex creation, roll up and vortex shedding) that sets the suction pressure distribution which dictates the instantaneous lift coefficient value. Because each solver had different characteristics (dynamics), these instants are not expected to be synchronized; they will happen at slightly different times because the effective dynamics captured by each solver is different. Moreover, the DDES and IDDES results are not perfectly repeatable due to the chaotic nature of the resolved turbulent scales. As a result, the timing of the selected snapshots are not exactly synchronized. This data sets the stage for the discussion.

A. URANS

The URANS solver is able to predict few features of the dynamic stall phenomenon. However, the accuracy and rich details of vigorous turbulence mixing are not evident in all the vorticity frames. Rather, we find a smooth, averaged, diffused vorticity distribution of the actual turbulent flow field. The first stage in the dynamic stall phenomenon is the creation of a LSB, which is evident in fig. 10a where the separation bubble is marked by rotating streamtraces. In parallel, flow reversal starts at the TE and propagates upstream across the airfoil suction surface. This stage sets the amount of vorticity fed by the LE shear layer into the LSB and the TE separated flow. Then, when the reversed flow reaches the LSB, it triggers the LSB eruption into a LEV, as shown in fig. 10d. Simultaneously, at the TE, the separated flow rolls up into a vortex structure, named the Trailing Edge Separated Vortex (TESV). At this moment, the LE separated shear layer is only feeding the LEV, and has no role in the dynamics of the TESV. In fact, the strength of the TESV depends on the amount of vorticity that has been hitherto fed into the trailing separated flow. The presented feeding dynamics emphasizes the importance of the first stage, as the strength of the TESV and the LEV are dictated at this stage. Also, these two vortices, the LEV and the TESV, do not seem to interact with each other. The pressure coefficient of these two frames could be found in fig. 11a, where a clear evidence of the LSB and LEV suction pressure is present. Interestingly, despite the presence of the TESV, it is not strong enough to induce powerful suction near the trailing edge, as shown in fig. 11a. The lift coefficient for the frames figs. 10a and 10d is shown in fig. 12a (Multimedia available online) with the second frame marking a sudden increase in the slope of the lift coefficient, which points to the LEV creation.

Marching further in time, the LEV continues to grow while being fed by the LE shear layer, as shown in fig. 10g. Also, the LEV convects downstream while being attached to the airfoil suction surface. On the other hand, the TESV does not maintain its position over the airfoil upper surface and sheds away into the wake, which diminishes its role in the ensuing events of the dynamic stall phenomenon. So, the LEV alone dominates the suction pressure coefficient during this phase, as shown in fig. 11a, which results in the maximum lift coefficient over the cycle presented in fig. 12a. However, the magnitude and timing of this maximum value do not match the experimental results. The obtained value of the maximum lift coefficient is smaller than the experimental one and is attained at a noticeably earlier time than the experiment. Another prominent contributor to the flow dynamics during this phase is the positive-vorticity shear layer emanating from the airfoil lower surface at the TE. This shear layer creates a strong vortex that is attached to the airfoil upper surface, as shown in fig. 10j, called Trailing Edge Vortex (TEV). This counter clockwise vortex formation, along with the shedding of the LEV from the airfoil upper surface, are responsible for the sudden loss of lift present in fig. 12a. Also, the effect of the LEV on the pressure coefficient curve in fig. 11a is not evident at this moment, however, there is a very strong suction peak near the

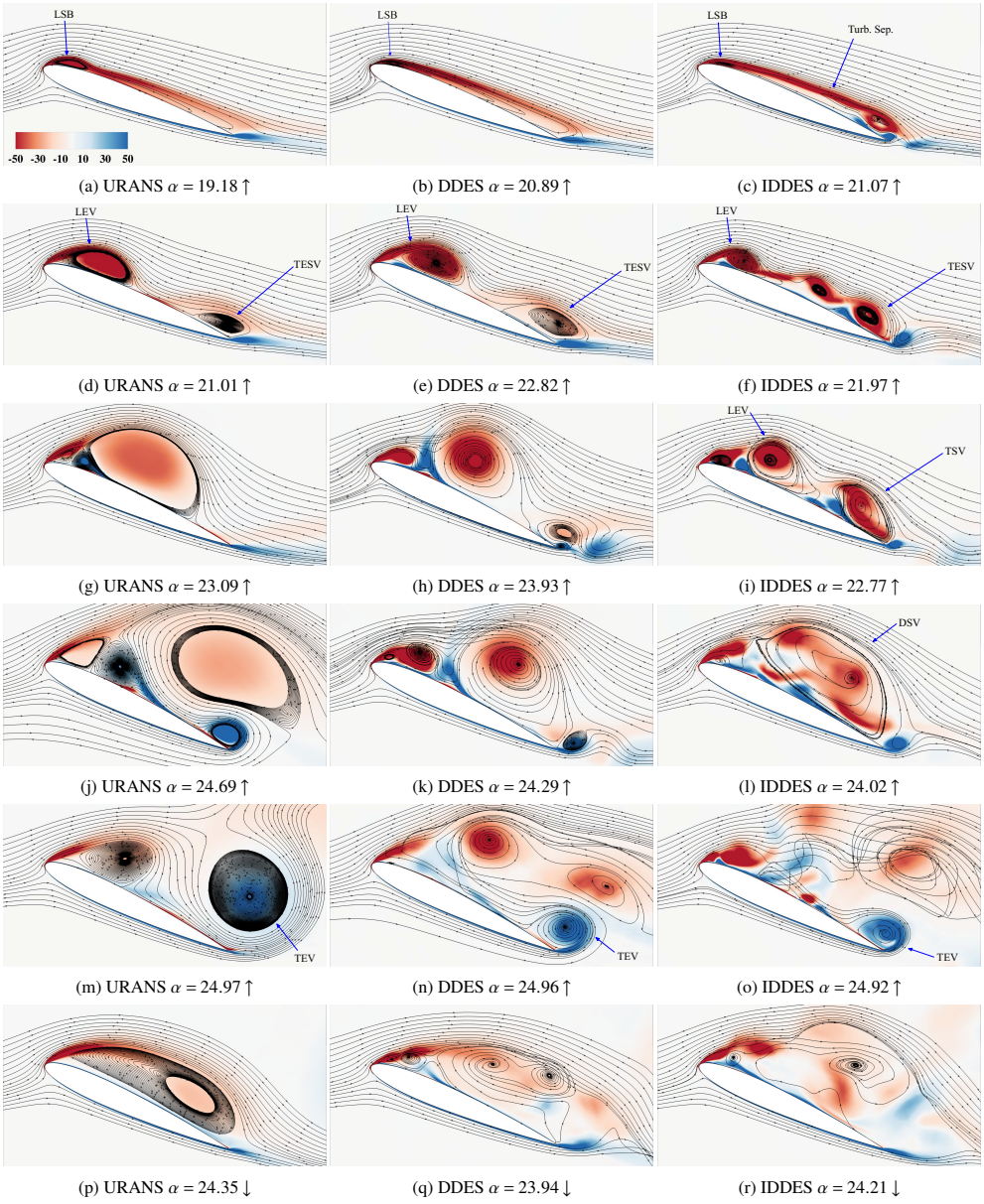

(a) URANS $\alpha = 19.18\uparrow$ (b) DDES $\alpha = 20.89\uparrow$ (c) IDDES $\alpha = 21.07\uparrow$

(d) URANS $\alpha = 21.01\uparrow$ (e) DDES $\alpha = 22.82\uparrow$ (f) IDDES $\alpha = 21.97\uparrow$

(g) URANS $\alpha = 23.09\uparrow$ (h) DDES $\alpha = 23.93\uparrow$ (i) IDDES $\alpha = 22.77\uparrow$

(j) URANS $\alpha = 24.69\uparrow$ (k) DDES $\alpha = 24.29\uparrow$ (l) IDDES $\alpha = 24.02\uparrow$

(m) URANS $\alpha = 24.97\uparrow$ (n) DDES $\alpha = 24.96\uparrow$ (o) IDDES $\alpha = 24.92\uparrow$

(p) URANS $\alpha = 24.35\downarrow$ (q) DDES $\alpha = 23.94\downarrow$ (r) IDDES $\alpha = 24.21\downarrow$

FIG. 10: Mid-plane z-vorticity contours along with streamtraces for all solvers presented in a chronological order. The left column is URANS; the middle is DDES and the right column is IDDES.

TE indicating the presence of the TEV. The next step shown in fig. 10m marks the maximum angle

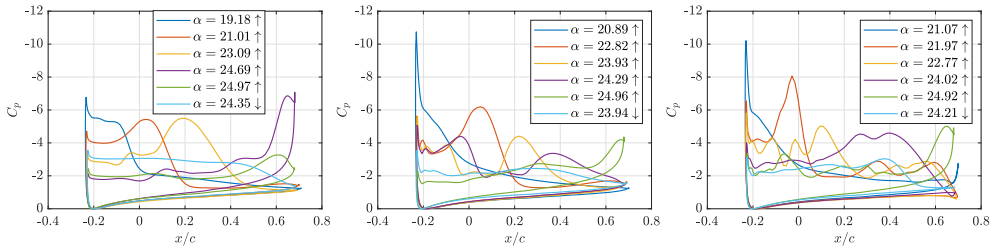

(a) URANS (b) DDES (c) IDDES

FIG. 11: Mid-plane pressure coefficient for presented frames in fig. 10.

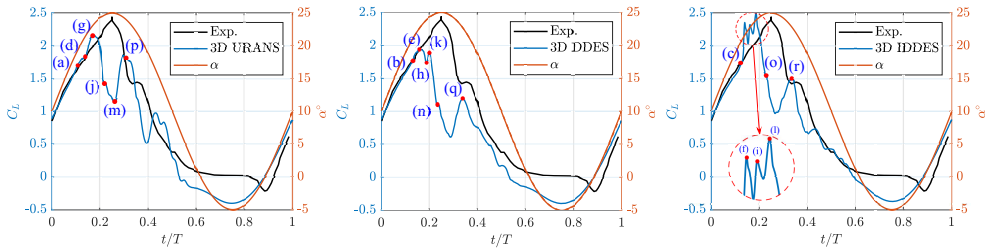

(a) URANS (Multimedia available online) (b) DDES (c) IDDES (Multimedia available online)

FIG. 12: Lift coefficient time history versus the experimental one along with the instantaneous angle of attack; each snapshot in fig. 10 is indicated by a lettered marker.

of attack over the cycle; the LEV is fully shed (i.e., out of the frame) and a grown TEV is separated from the airfoil surface downstream. This instant marks the minimum lift coefficient occurring at the upstroke cycle, and the corresponding pressure coefficient curve possesses the minimum suction all over the airfoil, as shown in fig. 11a. Meanwhile, there is an initiating vortex structure near the LE that receives vorticity from the LE shear layer; this vortex will constitute the Secondary LEV in the next frame. After the TEV sheds into the wake and convects downstream, the Secondary LEV dominates the scene, as evident in fig. 10p. The current predicted Secondary LEV possesses a deformed (i.e., squeezed) shape spanning the airfoil upper surface with a concentrated vorticity core near the TE. The squeezed appearance of the vortex is translated to a semi-uniform increase in the suction pressure over the airfoil, with slightly higher values near the TE, indicating the presence of the core, as shown in fig. 11a. However, similar to the main LEV, the URANS failed to predict the exact timing of the Secondary LEV along with the corresponding lift coefficient.

B. DDES

It is expected that the DDES solver will capture more details and mixing scales than the URANS—a fact that is clearly seen in fig. 10. For instance, in contrast to the smooth diffused vorticity contours found in URANS frames, DDES predicts a more resolved patches of vorticity. Similar to URANS behavior, at the beginning of the cycle, a LSB is formed and the reversed flow near the TE crawls upstream, as shown in fig. 10b. Simultaneously, both the LSB and the TE separated flow are fed with vorticity from the LE shear layer. This rich process takes place till the reversed flow collides with the LSB, at which the LSB erupts into a LEV, as shown in fig. 10e. At this stage, similar to URANS predictions, the LEV is attached to the airfoil upper surface, while the TE separated layer rolls up into a TESV structure. The pressure coefficient at these two consecutive snapshots is presented in fig. 11b, and the corresponding lift coefficients are shown in fig. 12b. The LSB effect, as well as the LEV, are represented as two distinct suction peaks in the pressure coefficient plots. Interestingly, the lift coefficient attains its maximum value over the cycle once the LEV is created, and there is no significant increase in the lift coefficient slope.

In next stage, as the airfoil continues pitching, fig. 10h shows the LEV detaching from the upper surface and convecting with the flow field. The LEV size is smaller than the one predicted by URANS, which results a concentrated peak suction over the airfoil upper surface, as shown in fig. 11b, in contrast to a spread suction distribution as predicted by URANS in fig. 11a. Also, at this instant, there is another peak in the suction curve near the LE, which indicates the rolling of an auxiliary smaller

LEV. These resolved vortex structures were not present in the URANS flow field, which implies that the DDES solver can resolve more scales than URANS. This resolution should have led to a better matching of the DDES lift coefficient with experimental data in comparison to the URANS results. Nevertheless, it turns out to be the opposite case because the DDES lift coefficient experiences a sudden decrease, as shown in fig. 12b. At the same snapshot, the TESV is convected downstream without considerably affecting the dynamic stall process. The next frame fig. 10k shows the LEV convecting downstream simultaneously with a growth of the auxiliary LEV. This growth induces a significant peak in the suction pressure coefficient near the LE, while the effect of the primary LEV over the suction pressure is diminishing due to its convection downstream. In turns, the lift coefficient slightly increases when compared to the previous frame values—a result that is attributed to the auxiliary LEV growth, though with quite inaccurate magnitude and peak timing compared to the experimental data. Moreover, at this frame, the initiation of the TEV is evident, whose effect will play a prominent role in the ensuing phase.

Approaching the end of the cycle, it is evident in fig. 10n that both LEVs have shed away and detached from the airfoil upper surface without any interaction. Meanwhile, the previously mentioned TEV has grown in size and strength. These two factors contribute to the suppression of the suction pressure coefficient, resulting in a sudden loss in the lift coefficient. Marching further in time, the continuously emanating shear layer from the LE rolls up to form the Secondary LEV, as shown in fig. 10q. Interestingly, the DDES solver is able to predict the correct timing of this vortex, but not its strength. Also, the pressure coefficient distribution has a notable peak implying the presence of the Secondary LEV, and identifying its location. In conclusion, the presented results of the DDES solver indicate its ability to capture more scales and resolving detailed spatial flow features compared to the URANS. However, it failed to predict the precise timing and magnitude of unsteady forces. This behavior could be attributed to the fact that the boundary layer dynamics is still resolved by the URANS and fed to the LES solver in the DDES simulation.

C. IDDES

The IDDES simulation results in the richest flow field compared to the other two solvers. Rich vorticity structures are evident in all frames, and vigorous turbulent mixing with various scales is captured, which contributes to the dynamic stall process. Following a similar chronological description as before, the creation of a LSB and the onset of flow reversal near the TE constitute the first stage in dynamic stall, as shown in fig. 10c. Although the IDDES results show similar LSB structures to those of the other solvers, it predicts a turbulent TE separated shear layer rather than a diffused one in contrast to the previous solvers. This TE separated shear layer will be refereed to as turbulent separation. The main reason behind this turbulent separation existence is the WMLES capturing and resolving the turbulent boundary layer and the adverse pressure causing the turbulent boundary layer to move forward. Moreover, the flow reversal is clearly present with a significant amount of distributed positive vorticity over the airfoil suction surface, which detaches the LE shear layer along with the turbulent separation from the airfoil suction surface. As such, larger amount of negative vorticity convect easily downstream causing a better nutrition process of the turbulent separation. In addition, the turbulent separation near the TE possesses a vortex like structure. This vortex structure is the initiation of the TESV, as will be seen in next frames. Most of these extra resolved features are present because the WMLES is resolving turbulent scales across the boundary layer, instead of averaging them as done within URANS and DDES. The LSB effect over the pressure coefficient along with the initiating vortex at the TE is distinguished in fig. 11c by two peaks in the suction side. Also, at this stage, the lift coefficient values attains excellent matching with the experimental data as seen in fig. 12c (Multimedia available online).

Then, fig. 10f shows that a LEV is created once the reversed flow reaches the LSB. In parallel, the TESV matures near the TE, and the LE shear layer is only feeding the LEV. Interestingly, there is another vortex created in between the LEV and the TESV. This middle vortex is of crucial importance because it helps the TESV hold its position near the TE instead of being washed away. These three vortex like structure will wrap up together to form the TSV structure and there presence aligns with the captured mechanism by Mulleners and Raffel [16]. Figure 11c shows the effect of these three vortices as three distinct peaks in the suction pressure values, which enhances the suction all over the airfoil upper surface and is translated as a spike in the lift coefficient value shown in fig. 12c. Unlike previous solvers, the TESV is not washed away instantly once created. However, it merges with the middle vortex (i.e., the vortex in between the LEV and TESV) to form the TSV, as shown in fig. 10i. Meanwhile, the LEV grows in size while convecting above the airfoil upper surface, and it contributes in maintaining the TSV position by attracting the TSV towards it. Simultaneously, another small LEV is created, which will be part of the DSV in the future instants. At this moment, most of the vorticity that has been fed by the LE shear layer either into the LEV or the turbulent separation, is present over the airfoil suction surface in the form of the LEV and the TSV. Also, if it were not for the middle vortex and the TESV, there would not have been a TSV. The presence of the TSV along with the LEV is clearly evident in the pressure coefficient results, and it clarifies the second spike in the lift coefficient values. The next frame in fig. 10l shows the most important stage of the dynamic stall process, which is the merging of the LEV and the TSV together to generate the DSV. Since this process is too rich to be duly presented by two snapshots only in figs. 10i and 10l, we provide a detailed sequence in fig. 13.

Figures 13a to 13e show a detailed dynamics of the TSV creation and the LEV shedding; figs. 13f to 13j present the merging process of different LE vortices with the TSV to form the DSV. Figure 13f clearly shows the complete formation of the TSV and the LEV, while the second auxiliary LEV is fed by the LE shear layer and grows in size. The next frame, fig. 13g, shows maturity of the second LEV while detaching

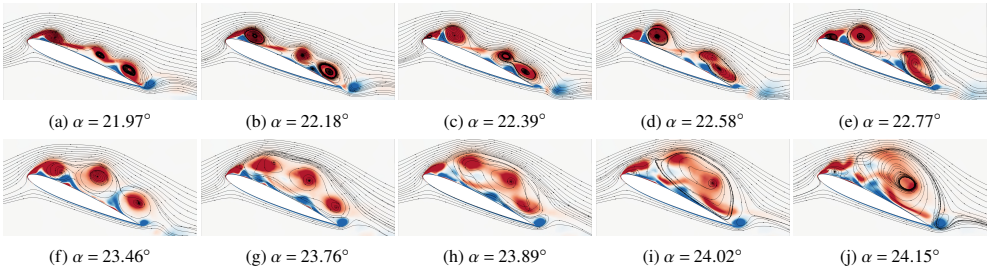

(a) $\alpha = 21.97°$ (b) $\alpha = 22.18°$ (c) $\alpha = 22.39°$ (d) $\alpha = 22.58°$ (e) $\alpha = 22.77°$

(f) $\alpha = 23.46°$ (g) $\alpha = 23.76°$ (h) $\alpha = 23.89°$ (i) $\alpha = 24.02°$ (j) $\alpha = 24.15°$

FIG. 13: LEV and TSV merging process to form the DSV in IDDES simulation

from the airfoil suction surface, in addition to the preliminary interaction between the TSV and the LEV. The interaction between the TSV and different LE vortices takes place across two different stages: (1) when the primary LEV is close enough to the TSV, it pulls the TSV towards it, hence the TSV is relocated underneath it, as shown in fig. 13h; and (2) as shown in fig. 13i, both the primary LEV and the TSV amalgamate to from a larger vortex—the DSV. Both steps take place while the auxiliary LEV is still present; and it interacts with the DSV in the ensuing phase. Once the DSV becomes strong enough, it pulls the second LEV towards it. They then roll together in a larger DSV that could be seen in fig. 13j. Having said that, the dominant role of the earlier stages becomes clear because they set the amount of vorticity that will eventually compose the DSV. Moreover, the presence of the TSV, middle vortex and the LEV along with their series of continuous merging is the fundamental mechanism to preserve the created vorticity by the LE shear layer over the suction surface for longer duration of the cycle. The Interaction between the the TSV, middle vortex and the LEV is the next key factor in dictating the position and strength of the DSV at initiation before conveting downstream, which is crucial for the prediction of lift coefficient histories throughout the unsteady motion. The DSV size and strength are translated as a wide spread suction in the pressure coefficient values, with the largest suction value compared to other solvers, as shown in fig. 11c. In turns, as presented in fig. 12c, the maximum lift coefficient all over the cycle is achieved at this frame. In fact, the IDDES simulation is the only solver that predicted nearly perfect lift coefficient history with an accurate maximum value over the cycle.

Inspecting fig. 10l where the DSV is created, there is a positive vorticity eddy near the TE which will form the TEV in next frame, fig. 10o. At this instant, the DSV diminishes and is fully washed away downstream of the airfoil. This shedding leads to a sudden loss in lift recorded in fig. 12c, and a significant suppression of the suction pressure coefficient over the airfoil. Figure 10r demonstrates the final step of the dynamic stall, which is the creation stage of the Secondary LEV. Interestingly, the IDDES accurately predicts both the timing and strength of the Secondary LEV, therefore, the resulting lift coefficient well matches the experimental data for this stage. In conclusion the results from the IDDES show the best agreement with experimental data in terms of lift in comparison to the previous two solvers. In particular, the maximum lift coefficient and its timing are accurately predicted. Also, the lift values corresponding to the Secondary LEV, and most of the downstroke, are nearly overlapping with the experimental data. Moreover, the IDDES simulation has the richest flow field features in comparison to the other solvers.

V. DISCUSSION

It is clear from the previous presented discussion that all three solvers share some of the dynamic stall features such as the LSB, flow reversal, LEV creation and convection, TESV presence and the Secondary LEV. However, the IDDES results are uniquely distinguished by the presence of the TSV—a vortex that was mainly captured because of the WMLES ability to resolve the turbulent boundary layer, which allowed various small eddies to constitute the TSV. This special vortex interacts with the LEV to form the DSV. Actually, the DSV creation process is not due to a single interaction between the LEV and TSV; it is a series of cascaded amalgamation events between the TSV and all the LEVs that are substantial for accurate prediction of the DSV, and consequently, the aerodynamic loads. This feature was not captured by the DDES, where two consecutive LEVs are created and shed without interaction. All these promising results of IDDES show that extra flow features that are captured by inherently three-dimensional solvers—LES and WMLES for turbulent boundary layer—are crucial for accurate prediction of dynamic stall and the associated lift dynamics.

The presented discussion showed multiple evidences supporting the argument about dynamic stall being a three-dimensional phenomenon. First, it was clear that a 3D simulation of a dynamic stall maneuver result in more accurate loads and flow features when compared to a 2D one, even within the relatively incapable URANS framework. Second, the extra resolved scales by LES in the free shear layer region resulted in richer flow field features in comparison to global averaging of turbulent scales—a characteristic that only DDES and IDDES possessed. Third, the WMLES (which is an inherently 3D modeling method) within the IDDES simulation captured the turbulent complex dynamics that is present over

the airfoil suction surface, which resulted in the most accurate flow features and aerodynamic loads in comparison to other simulations. In conclusion, dynamic stall should be studied in a three-dimensional formulation taking into account three-dimensional nature of the flow field even though the geometry of the problem is purely two-dimensional.

VI. CONCLUSION

The hypothesis that dynamic stall has a 3D nature was tested by performing different simulations (URANS, DDES and IDDES) for a pitching NACA 0012 airfoil. The results showed that the lift coefficient obtained from a 3D simulation was in better agreement with the experimental data when compared to that obtained from a 2D simulation. Due to averaging of turbulent scales, the URANS failed to predict prominent features of the dynamic stall phenomenon, which consequently led to a mismatch between the numerical and experimental lift coefficient magnitude at the maximum value and the start of downstroke. In contrast, the DDES and IDDES, had a better performance than URANS. The LES solver in both of them captured extra turbulent scales across the flow field, with a remarkable increase within the IDDES due to WMLES. The complex dynamics of the DSV creation presented in the interaction between multiple LEVs and the TSV was only evident within the IDDES simulation, leading to exact matching of the numerical lift coefficient time histories with the experimental data throughout 85% of the cycle. All the resulting facts supported the argument that, even though the dynamic stall is studied for a 2D infinite-airfoil, the flow physics are inherently 3D in nature. This fact implies that the dynamic stall phenomenon is intrinsically three-dimensional.

ACKNOWLEDGMENT

This work was supported by the National Science Foundation (NSF) grant numbers CMMI-1846308 and CBET-2005541.

[1] M. R. Visbal and D. J. Garmann, "Analysis of dynamic stall on a pitching airfoil using high-fidelity large-eddy simulations," AIAA Journal **56**, 46–63 (2018).
[2] W. J. McCroskey, L. W. Carr, and K. W. McAlister, "Dynamic stall experiments on oscillating airfoils," Aiaa Journal **14**, 57–63 (1976).
[3] W. J. McCroskey, "The phenomenon of dynamic stall." Tech. Rep. (National Aeronuatics and Space Administration Moffett Field Ca Ames Research . . . , 1981).
[4] W. J. McCroskey, "Unsteady airfoils," Annual review of fluid mechanics **14**, 285–311 (1982).
[5] L. W. Carr, "Progress in analysis and prediction of dynamic stall," Journal of aircraft **25**, 6–17 (1988).
[6] M. R. Visbal, "Analysis of the onset of dynamic stall using high-fidelity large-eddy simulations," in *52nd Aerospace Sciences Meeting* (2014) p. 0591.
[7] M. R. Visbal and D. J. Garmann, "Investigation of spanwise end effects on dynamic stall of a pitching wing section," Journal of Aircraft **56**, 2118–2130 (2019).
[8] R. Gupta and P. J. Ansell, "Investigation of the effects of reynolds number on the unsteady flow physics of airfoil dynamic stall," in *2018 AIAA Aerospace Sciences Meeting* (2018) p. 0354.
[9] H. E. Taha, L. P. Olea, N. Khalifa, C. Gonzalez, and A. S. Rezaei, "Geometric-control formulation and averaging analysis of the unsteady aerodynamics of a wing with oscillatory controls," Journal of Fluid Mechanics **928** (2021).
[10] L. Pla Olea, N. M. Khalifa, and H. E. Taha, "Geometric control study of the beddoes-leishman model in a pitching-plunging airfoil," in *AIAA SCITECH 2022 Forum* (2022) p. 2415.
[11] G. J. Leishman, *Principles of helicopter aerodynamics with CD extra* (Cambridge university press, 2006).
[12] J. W. Larsen, S. R. Nielsen, and S. Krenk, "Dynamic stall model for wind turbine airfoils," Journal of Fluids and Structures **23**, 959–982 (2007).
[13] C. R. dos Santos, D. R. Pacheco, H. E. Taha, and M. Y. Zakaria, "Nonlinear modeling of electro-aeroelastic dynamics of composite beams with piezoelectric coupling," Composite Structures **255**, 112968 (2021).
[14] D. Deb, P. Shetty, K. Poddar, and S. Kumar, "Flow induced oscillation of two rigid rectangular plates in a side-by-side configuration," Journal of Fluids and Structures **99**, 103133 (2020).
[15] A. I. El-Nadi, N. M. Khalifa, and H. E. Taha, "Compressible unsteady aerodynamic loads on oscillating airfoils in a subsonic flow," in *AIAA SCITECH 2022 Forum* (2022) p. 1980.
[16] K. Mulleners and M. Raffel, "Dynamic stall development," Experiments in fluids **54**, 1–9 (2013).
[17] T. Lee and P. Gerontakos, "Investigation of flow over an oscillating airfoil," Journal of Fluid Mechanics **512**, 313–341 (2004).
[18] S. Wang, D. B. Ingham, L. Ma, M. Pourkashanian, and Z. Tao, "Numerical investigations on dynamic stall of low reynolds number flow around oscillating airfoils," Computers & fluids **39**, 1529–1541 (2010).
[19] S. Wang, D. B. Ingham, L. Ma, M. Pourkashanian, and Z. Tao, "Turbulence modeling of deep dynamic stall at relatively low reynolds number," Journal of Fluids and Structures **33**, 191–209 (2012).
[20] K. Gharali and D. A. Johnson, "Dynamic stall simulation of a pitching airfoil under unsteady freestream velocity," Journal of Fluids and Structures **42**, 228–244 (2013).
[21] K. Singh and J. C. Páscoa, "Numerical modeling of stall and poststall events of a single pitching blade of a cycloidal rotor," Journal of Fluids Engineering **141** (2019).
[22] S. Benton and M. Visbal, "The onset of dynamic stall at a high, transitional reynolds number," Journal of Fluid Mechanics **861**, 860–885 (2019).
[23] K. Mulleners and M. Raffel, "The onset of dynamic stall revisited," Experiments in fluids **52**, 779–793 (2012).
[24] B. J. Pruski and R. Bowersox, "Leading-edge flow structure of a dynamically pitching naca 0012 airfoil," AIAA journal **51**, 1042–1053 (2013).
[25] J. Larsson, S. Kawai, J. Bodart, and I. Bermejo-Moreno, "Large eddy simulation with modeled wall-stress: recent progress and future directions," Mechanical Engineering Reviews **3**, 15–00418 (2016).
[26] S. B. Pope, "Turbulent flows," (2001).
[27] D. C. Wilcox *et al.*, *Turbulence modeling for CFD*, Vol. 2 (DCW industries La Canada, CA, 1998).
[28] P. R. Spalart, "Comments on the feasibility of les for wings, and on a hybrid rans/les approach," in *Proceedings of first AFOSR international conference on DNS/LES* (Greyden Press, 1997).
[29] J. L. Petrilli, R. C. Paul, A. Gopalarathnam, and N. T. Frink, "A cfd database for airfoils and wings at post-stall angles of attack," in *31st AIAA Applied Aerodynamics Conference* (2013) p. 2916.
[30] K. A. Goc, O. Lehmkuhl, G. I. Park, S. T. Bose, and P. Moin, "Large eddy simulation of aircraft at affordable cost: a milestone in computational fluid dynamics," Flow **1** (2021).
[31] P. Sagaut, *Large eddy simulation for incompressible flows: an introduction* (Springer Science & Business Media, 2006).
[32] H. Schlichting, K. Gersten, E. Krause, H. Oertel, and K. Mayes, *Boundary-layer theory*, Vol. 7 (Springer, 1960).
[33] M. Shur, P. Spalart, M. Strelets, and A. Travin, "Detached-eddy simulation of an airfoil at high angle of attack," in *Engineering turbulence modelling and experiments 4* (Elsevier, 1999) pp. 669–678.
[34] P. R. Spalart, "Strategies for turbulence modelling and simulations," International Journal of Heat and Fluid Flow **21**, 252–263 (2000).
[35] A. Travin, M. Shur, M. Strelets, and P. Spalart, "Detached-eddy simulations past a circular cylinder," Flow, turbulence and combustion **63**, 293–313 (2000).

[36]M. Strelets, "Detached eddy simulation of massively separated flows," in *39th Aerospace sciences meeting and exhibit* (2001) p. 879.
[37]U. Bunge, C. Mockett, and F. Thiele, "Guidelines for implementing detached-eddy simulation using different models," Aerospace Science and Technology **11**, 376–385 (2007).
[38]H. Tennekes and J. L. Lumley, *A first course in turbulence* (MIT press, 2018).
[39]F. Menter and M. Kuntz, "Adaptation of eddy-viscosity turbulence models to unsteady separated flow behind vehicles," in *The aerodynamics of heavy vehicles: trucks, buses, and trains* (Springer, 2004) pp. 339–352.
[40]P. R. Spalart, S. Deck, M. L. Shur, K. D. Squires, M. K. Strelets, and A. Travin, "A new version of detached-eddy simulation, resistant to ambiguous grid densities," Theoretical and computational fluid dynamics **20**, 181 (2006).
[41]M. L. Shur, P. R. Spalart, M. K. Strelets, and A. K. Travin, "A hybrid rans-les approach with delayed-des and wall-modelled les capabilities," International Journal of Heat and Fluid Flow **29**, 1638–1649 (2008).
[42]A. K. Travin, M. L. Shur, P. R. Spalart, and M. K. Strelets, "Improvement of delayed detached-eddy simulation for les with wall modelling," (2006).
[43]N. Nikitin, F. Nicoud, B. Wasistho, K. Squires, and P. R. Spalart, "An approach to wall modeling in large-eddy simulations," Physics of fluids **12**, 1629–1632 (2000).
[44]P. R. Spalart, "Detached-eddy simulation," Annual review of fluid mechanics **41**, 181–202 (2009).
[45]C. Mockett, *A Comprehensive Study of Detached Eddy Simulation* (Universlagtuberlin, 2009).
[46]P. Spalart and S. Allmaras, "A one-equation turbulence model for aerodynamic flows," in *30th aerospace sciences meeting and exhibit* (1992) p. 439.
[47]F. R. Menter, "Two-equation eddy-viscosity turbulence models for engineering applications," AIAA journal **32**, 1598–1605 (1994).
[48]D. C. Wilcox, "Formulation of the kw turbulence model revisited," AIAA journal **46**, 2823–2838 (2008).
[49]A. Travin, M. Shur, M. Strelets, and P. Spalart, "Physical and numerical upgrades in the detached-eddy simulation of complex turbulent flows," in *Advances in LES of complex flows* (Springer, 2002) pp. 239–254.
[50]M. S. Gritskevich, A. V. Garbaruk, J. Schütze, and F. R. Menter, "Development of ddes and iddes formulations for the k-ω shear stress transport model," Flow, turbulence and combustion **88**, 431–449 (2012).
[51]G. Martinat, M. Braza, Y. Hoarau, and G. Harran, "Turbulence modelling of the flow past a pitching naca0012 airfoil at 105 and 106 reynolds numbers," Journal of Fluids and Structures **24**, 1294–1303 (2008).
[52]K. W. McAlister, L. W. Carr, and W. J. McCroskey, "Dynamic stall experiments on the naca 0012 airfoil," Tech. Rep. (1978).
[53]N. M. Khalifa, A. S. Rezaei, and H. E. Taha, "Comparing the performance of different turbulence models in predicting dynamic stall," in *AIAA Scitech 2021 Forum* (2021) p. 1651.
[54]F. R. Menter, "Best practice: scale-resolving simulations in ansys cfd," ANSYS Germany GmbH **1** (2012).
[55]A. Kozelkov, V. Kurulin, V. Emelyanov, E. Tyatyushkina, and K. Volkov, "Comparison of convective flux discretization schemes in detached-eddy simulation of turbulent flows on unstructured meshes," Journal of Scientific Computing **67**, 176–191 (2016).
[56]P. R. Spalart and C. Streett, "Young-person's guide to detached-eddy simulation grids," (2001).
[57]F. M. Najjar and S. P. Vanka, "Effects of intrinsic three-dimensionality on the drag characteristics of a normal flat plate," Physics of fluids **7**, 2516–2518 (1995).
[58]C. C. Critzos, H. H. Heyson, and R. W. Boswinkle Jr, "Aerodynamic characteristics of naca 0012 airfoil section at angles of attack from 0 deg to 180 deg," Tech. Rep. (NATIONAL AERONAUTICS AND SPACE ADMINISTRATION WASHINGTON DC, 1955).
[59]R. M. Cummings, S. A. Morton, and D. R. McDaniel, "Experiences in accurately predicting time-dependent flows," Progress in Aerospace Sciences **44**, 241–257 (2008).
[60]Y. Qin, Q. Qu, P. Liu, Y. Tian, and Z. Lu, "Dde study of the aerodynamic forces and flow physics of a delta wing in static ground effect," Aerospace Science and Technology **43**, 423–436 (2015).
[61]H. JCR, A. Wray, and P. Moin, "Eddies, stream, and convergence zones in turbulent flows," Studying Turbulence Using Numerical Simulation Databases-I1 **193** (1988).
[62]M. Fouda, N. M. Khalifa, M. M. Rashad, M. Shao, M. Elsharif, and H. E. Taha, "Static and dynamic characteristics of the aerodynamic forces on pitching airfoils between 0 to 360 degrees angle of attack," in *AIAA SCITECH 2022 Forum* (2022) p. 1663.